Published as: Power Supply based on Inductive Harvesting from Structural Currents, IEEE Internet of Things Journal, doi: 10.1109/JIOT.2021.3086013
https://ieeexplore.ieee.org/document/9446497

Power Supply based on Inductive Harvesting from Structural Currents

Michail. E. Kiziroglou, *Senior Member, IEEE*, Steven W. Wright and Eric M. Yeatman, *Fellow, IEEE*

Abstract- **Monitoring infrastructure offers functional optimisation, lower maintenance cost, security, stability and data analysis benefits. Sensor nodes require some level of energy autonomy for reliable and cost-effective operation, and energy harvesting methods have been developed in the last two decades for this purpose. Here, a power supply that collects, stores and delivers regulated power from the stray magnetic field of current-carrying structures is presented. In cm-scale structures the skin effect concentrates current at edges at frequencies even below 1 kHz. A coil-core inductive transducer is designed. A flux-funnelling soft magnetic core shape is used, multiplying power density by the square of funnelling ratio. A power management circuit combining reactance cancellation, voltage doubling, rectification, super-capacitor storage and switched inductor voltage boosting and regulation is introduced. The power supply is characterised in house and on a full-size industrial setup, demonstrating a power reception density of 0.36 mW/cm^3, 0.54 mW/cm^3 and 0.73 mW/cm^3 from a 25 A RMS structural current at 360 Hz, 500 Hz and 800 Hz respectively, corresponding to the frequency range of aircraft currents. The regulated output is tested under various loads and cold starting is demonstrated. The introduced method may enable power autonomy to wireless sensors deployed in current-carrying infrastructure.**

Index Terms**—Energy harvesting, Inductive Transducers, Sensor Systems, Aircraft.**

I. Introduction

Energy harvesting can be described as the seamless collection of environmental energy to provide a power source for local use. It has the potential of enabling power autonomy to systems that are otherwise already physically untethered. During the last twenty years, a wealth of energy harvesting concepts has been developed, mainly employing piezoelectric, electrostatic and electromagnetic transduction for motion energy sources, thermoelectric devices for heat, rectennas for Radio Frequency (RF) electromagnetic waves and solar cells for light. In a lot of cases, power densities sufficient for supporting wireless sensor microsystems have been demonstrated. For example, in [1] Reilly et al demonstrated an autonomous wireless sensor, able to operate at 0.2% duty cycle while powered from a 100 Hz, 0.25 g vibration, through a 6.75 cm^2 piezoelectric transducer. In [2], von Allmen et al presented an aircraft strain sampling sensor node operating at 4.5% duty cycle for 800 s, powered by temperature fluctuation during a flight, through a 9 cm^2 thermoelectric generator and 23 g of water used for heat storage. Reviews presenting recent advances of piezoelectric [3, 4], acoustic [5], thermal [6] and RF [7] energy harvesting devices, can be found in the literature.

Manuscript received March 9, 2021; revised April 27, 2021; accepted May 27 2021; date of publication …; date of current version.... This work has received funding from the Clean Sky 2 Joint Undertaking under the European Union's Horizon 2020 research and innovation programme grant No 785495 and Project AMPWISE.
M. E. Kiziroglou, S. W. Wright and E. M. Yeatman are with the Department of Electrical and Electronic Engineering, Imperial College London, SW7 2AZ, U.K. (e-mail: m.kiziroglou@ic.ac.uk)
M. E. Kiziroglou is also with the Department of Industrial Engineering and Management, International Hellenic University, 57400, Greece.

Power management systems convert the energy harvesting transducer output into a form suitable for the intended energy user, e.g. for the microcontroller of a wireless sensor node. Conversion requirements include rectification, voltage level translation, impedance matching, buffering and regulation. These features are implemented by a combination of rectifiers, switched inductor boost and buck converters, intermediate storage into a battery and/or supercapacitor, maximum power point tracking, component protection and other control circuitry. A list of some common commercial integrated power management microchips is show in Table I.

TABLE I
COMMERCIAL POWER MANAGEMENT INTEGRATED CIRCUITS

Model	Bipolar	Cold Start Threshold / V	MPPT	Features
BQ25505 [8]	NO	0.33	YES	boost / store
BQ25570 [9]	NO	0.6	YES	boost / store / reg
LTC3109 [10]	YES	0.03	NO	boost / store / reg
LTC3588-1[11]	YES	4	NO	store/reg

The efficient combination of bipolar input and low cold-starting voltage capability is challenging due to diode voltage drop in passive rectifiers. The switched transformer approach followed in LTC3109 offers a unique cold-starting voltage of 30 mV, though at low efficiency [10]. A different coupled inductor approach has also become available as an application specific integrated circuit (ASIC), with higher reported efficiency at similar input voltage [12, 13]. A different approach employing a passive Schottky diode rectifier combined with an optimised synchronised active transistor circuit has been introduced in [14]. An overview of power management methods for energy harvesting can be found in [15].

An energy harvesting concept that combines environmental power availability and locations of interest for infrastructure monitoring is coupling to power lines and other alternating current (AC) carrying structures. Environments involving electrical currents include industrial plant areas, large machinery, power distribution lines, electrical installations of buildings and vehicle power networks. Piezoelectric [16-22] electrostatic [23-26], and inductive [27-34] coupling methods have already been studied for this purpose, demonstrating that adequate power density can be achieved by non-invasive coupling, to support wireless sensors with continuous power.

An application environment of special interest for this concept is that of aircraft. The electrical power network of aircraft involves currents as high as 100 A Root-Mean-Square (RMS),

at a 360 Hz – 800 Hz frequency range which is beneficial for inductive coupling. The aircraft structural beams are used as the return current path. Therefore, one-way current flow is available in various locations, allowing a significant alternating magnetic field to occur around structural beams as well as around power harnesses. This environment offers an opportunity for lightweight, autonomous sensors, which are particularly attractive due to the critical role of weight and infrastructure complexity on aircraft.

In previous work, a power line harvesting method for aircraft power lines was developed demonstrating 0.6 mW/cm^3 from a 0.9 A RMS, 650 Hz current. The effect of current distribution in current-carrying structures, including the skin effect [35] was studied in [36]. The use of flux funnelling magnetic soft-core shapes was also proposed in [36], showing a potential power density increase by a factor of 50. Other previously reported flux guiding techniques for power line energy harvesting include a bow-tie shaped core geometry [30] and the U-shaped flux guides employed in [29]. Furthermore, the optimisation of coil/core design was studied in [37], revealing a two-fold further power density improvement, by selecting the optimal coil/core mass balance.

In this paper, an autonomous power supply is presented, based on inductive energy harvesting from the magnetic field of current-carrying structures. It comprises a core-and-coil transducer with flux-funnelling geometry and optimized core/coil mass balance based on the methods introduced in [36] and [37], a voltage-doubling rectifier, two supercapacitor energy storage units and a commercial integrated switched-inductor voltage booster. Laboratory experimental results using an emulated distributed current testing setup are presented, emphasizing on cold-starting performance, with and without a dissipative load at the power supply output. Further experimental results from performance evaluation tests on an industrially-developed aircraft beam testing setup are also presented, and the potential for magnetic field powered sensors is discussed for aircraft and other industrial applications.

The remaining of this paper is organized as follows. The energy harvesting concept is described in Section II. The transducer design and optimization method is briefly reviewed in Section III. The power management and storage circuit is discussed in Section IV. In Sections V and VI, experimental results from laboratory and industrial tests are presented and analysed, including details of the testing methods used. Finally, conclusions and an outlook for using the power supply in wireless aircraft sensors are discussed in Section VII.

II. The Inductive Power Line Harvesting Concept

When an AC current is flowing through a power line or through a structure, energy can be collected by a coil coupled to the varying magnetic field through the electromagnetic induction effect. This concept is similar to that of an electric transformer, but has two important design objective differences. First, as the primary current is typically part of a separate infrastructure, a minimally invasive design is critical, in order to observe specific constraints and achieve a seamless and practical installation. Second, maximum power density is typically a priority in energy harvesting applications. Therefore, the coil and core structure must be designed to operate at its maximum output power point. In turn this leads to a performance that is largely defined by the output impedance of the coil.

The concept of energy harvesting from structural currents is illustrated in Fig. 1, using an H-shape cross-section beam as an example. The AC current flow runs along the beam length with a density J. Even in the 50 Hz – 1 kHz frequency range, the current distribution is uneven due to the skin effect, which pushes the current to the beam edges. In turn, this increases the magnetic field at the edge locations, offering locations that are beneficial for installing an inductive harvester. The importance of this effect on device performance has been studied in [36, 37]. Furthermore, a soft magnetic core can be used to enhance the magnetic flux density B through a coil. A funnel-shaped core can be used to concentrate flux and pass it through a thinner coil, thereby reducing core mass, coil mass and coil length which in turn leads to a lower coil resistance. A conceptual 3D model of such a coil-core harvester design is illustrated in Fig. 1. In this way, the power density can scale up with the square of the flux funnelling geometrical ratio, in the linear soft core polarization range. This concept has been introduced in [36] and studied in [37], showing a potential fifty-fold power density increase for a 1:8 funnelling ratio.

Furthermore, an optimal core/coil mass balance exists, at which the total transducer power density is maximised. This has been demonstrated in [37], offering a design method for coil-core transducers used as power receivers for energy harvesting or inductive power transfer. For a given total transducer mass allowance, a practical core size and funnelling ratio is selected, the number of coil turns is defined to achieve a convenient output voltage range for the given available environmental B, and the coil wire diameter is defined to achieve the mass balance that provides the maximum power density.

Finally, the reactive part of the coil output impedance can be cancelled by a passive impedance cancellation circuit. This can be implemented by a single series capacitor for a certain operation frequency. For broadband operation, a more complex reactance network can be employed, at the expense of additional resistive losses. Self-tuning approaches may also be considered for this purpose.

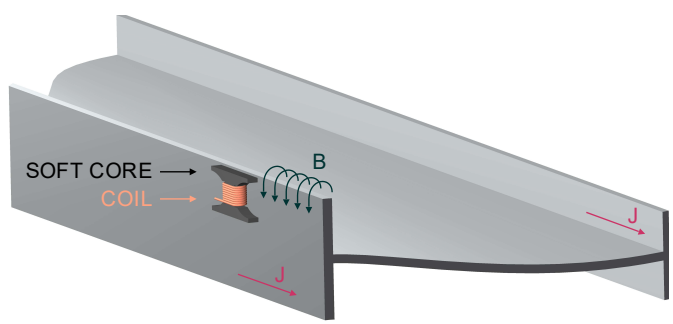

Fig. 1: Illustration of inductive harvesting from a current-carrying structural beam, using a flux funnelling soft magnetic core.

The maximum output power density P_D is then achieved at impedance matching conditions (including reactance cancellation), which can be written as a function of the real part R_C of the coil impedance, open circuit voltage amplitude V_o and total transducer mass m as:

$$P_D = \frac{V_o^2}{8mR_C} \quad (1)$$

III. Transducer Design and Fabrication

The coil and core inductive transducer of the energy harvesting power supply introduced in this paper was designed following the method introduced [37] as outlined in Section II. An industrially-defined sensing use case was assumed, involving the deployment of energy autonomous current sensor nodes with continuous power requirement in the 0.1 mW – 1 mW range. The sensors are deployed on aircraft structural beams carrying AC currents up to 100 A RMS, in the 360 Hz – 800 Hz frequency range. This corresponds to a magnetic flux density range up to 1 mT RMS, at the beam cross-section edges. A current distribution and magnetic field simulation study can be found in [37] and in Section V.A. of this paper, where the laboratory testing setup is developed and configured accordingly. A total sensor node mass maximum limit of 50 g was defined.

In order to obtain a convenient output voltage range from the given flux density characteristics, Cu coils of 10,000 turns were designed, and fabricated as a customised batch by North Devon Electronics Ltd. The coil length, inside and outside diameter are 20 mm, 5 mm and 11 mm respectively. A coil wire diameter of 60 µm was chosen, following the approach discussed in Section II. A fitting 5 mm diameter cylindrical ferrite rod with a 250 nominal specific permeability was installed through the coil, flanked by two high-permeability, 0.15 × 5 × 40 mm flanges, forming a flux-funnelling H-structure. The flanges were fabricated by lamination of 5 layers of a 30 µm thick nanocrystalline thin ferrite film. The total mass of the coil and the assembled core were measured to be 6.7 g and 2.4 g respectively, resulting in a 9.1 g transducer. An overview of the transducer structure and dimensions is presented in Fig. 2. A photograph of the coil and the cylindrical ferrite core is shown in the inset.

IV. Power Management and Storage

A power management system comprising reactance cancellation, rectification, energy storage, overvoltage protection, voltage boosting and regulation was developed, in order to integrate the energy harvesting transducer into a functional power supply. A block diagram of this architecture is illustrated in Fig. 3a. A circuit implementing this approach is presented in Fig. 3b. Reactance cancellation is achieved by a single capacitor C_S connected in series with the coil and selected to present a negative reactance of equal magnitude with that of the coil.

The rectification stage consists of a two-stage Dickson charge pump rectifier, employing Schottky diodes to minimize voltage drop, and allow cold-starting from coil voltage outputs V_{COIL} below 1 V. The Panasonic DB2730800L Schottky diode model was selected for this purpose, because of its low forward bias voltage drop (0.2 V at 1.5 mA) and its low reverse bias leakage (2 µA at 5 V) [38]. A super-capacitor, C_1 is employed as the main energy storage unit of the power supply, connected at the output of the rectifying bridge. The C_S, half-bridge and C_1 components form a voltage doubling topology [39]: In the negative semi-period of V_{COIL}, C_S is reverse-charged through the first diode (vertical D_S in Fig. 3b). This C_S voltage is added to V_{COIL} during the positive semi-period, allowing a higher voltage output to be applied to C_1 through the second diode (horizontal D_S in Fig. 3b). Thereby, C_1 is gradually charged towards a value of $2V_{COIL}$. In practice this is an asymptotic value, due to the increasing diode voltage drop as the current is gradually reduced.

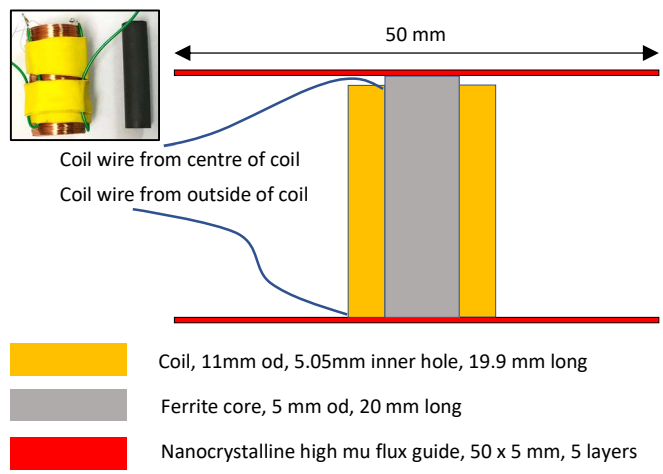

Fig. 2: Illustration of the transducer structure and dimensions. A picture of the coil with its cylindrical core part is shown on the top left as an inset.

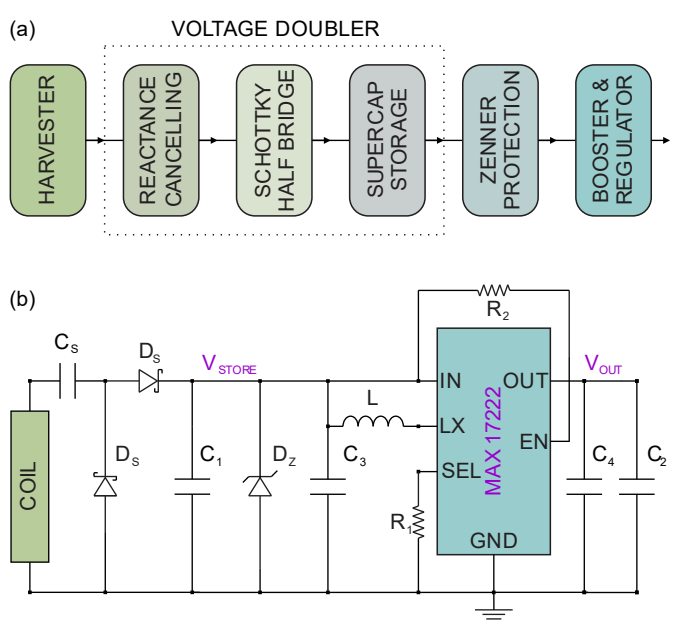

Fig. 3: (a) Block diagram of the power management and storage system. (b) Circuit schematic.

A Zener diode is connected in parallel to C_1, to protect both the supercapacitor storage and the subsequent booster circuit input from voltages exceeding their specifications. A commercial switched inductor L circuit is used for voltage boosting and regulation. In the implementation of Fig. 3b, a MAXIM 17222 chip is employed, with a selectable output voltage range between 1.8 V and 5 V, through the resistor R_1. The capacitors C_3 and C_4 are connected to the chip input and output to provide the minimum required capacitance. Its chip-enable signal of the chip is connected to the input pin through a resistor R_2. The self-starting input voltage threshold of this chip is 0.88 V, and it can thence operate with input voltages as low as 0.40 V (nominally). A maximum output current of 0.5 A can be supplied to the output from this chip. Specifications and further details of the operation and performance of this boosting and regulation solution can be found in [40]. A secondary energy storage capacitor, C_2 is included in parallel to C_4 at the system output, as a power buffer to accommodate power demand bursts.

The circuit of Fig. 3b was implemented on a 20 mm × 30 mm printed circuit board (PCB) with the components summarised in Table II. The PCB was printed by JLCPCB and home soldered using a C.I.F. Tecprint 700 manual stencil printer and a C.I.F. FT05 reflow oven. External components were used for C_S to allow its variation during reactance cancellation experiments. The R_1 value was selected to enable a 3.3 V regulated output. A separate PCB with $R_1 = 0\ \Omega$ for 1.8 V was also fabricated and used during tests. The storage capacitors C_1 and C_2 were connected externally. External connections were made through two 12-pin 2.54 mm pitch female connectors soldered on the PCB, selected to allow multiple connections for testing convenience.

TABLE II
COMPONENTS USED FOR IMPLEMENTING THE CIRCUIT OF FIG. 3B

Symbol	Value	Model	Notes
C_S	4 – 40 nF	-	Reactance Cancellation
D_S	0.21 V @ 2 mA	Panasonic DB27308	Reverse: 2 µA @ 2.5 V.
Dz	5.6 V	Vishay BZD27C5V6P	800 mW
C_1	0.47 F	AVX SCMR14D474PSBB0H	External
C_2	1 mF	Rubycon Al Electrolytic	External
C_3, C_4	10 µF	Murata GRM Series	Multilayer Ceramic
L	3.3 mH	Wurth Elektronik PMI Series	Multilayer
R_1	80.6 kΩ	Panasonic ERJ8EN Series	Thick film
R_2	33 MΩ	Multicomp Pro HVR Series	Thick film

The coil, the soft core structure, the PCB and the storage capacitors were integrated with the help of a custom-designed, 3D printed Acrylonitrile butadiene styrene (ABS) box. The box includes a concave pedestal for the coil, slots for the thin soft magnetic core flanges, and fitting space for the C_1 supercapacitor and the PCB on either side of the coil. A photograph of the complete power supply assembly is shown in Fig. 4, including a view of the power management PCB in the inset.

The overall outer dimensions of power supply package shown in Fig. 4 are 75 × 23 × 17 mm. A summary of the mass for each component is provided in Table III, with a total of 27.8 g.

TABLE III
MASS OF THE DIFFERENT POWER SUPPLY COMPONENTS

Component	Value / g
Coil	6.7
Core	2.4
PCB	6
Supercapacitors	5.5
Box (ABS)	7.2
Total	27.8

V. LABORATORY TESTING

A. *Description of home testing setup.*

To characterize the performance of the power supply under realistic conditions, the application case of an aircraft structural beam is employed. Structural beams are used as the current return path of aircraft electrical power networks, which involve AC components of variable frequency in the 360 – 800 Hz range. Depending on size and geometry, the skin effect can push current flow to the edges, creating areas of increased B around them. The specific, H – cross-section beam shown in Fig. 5 is considered. Numerical, 3D simulations for a 1 A amplitude current are shown in Fig. 6, illustrating the spatial J and B distributions. An extended simulation study and analysis of this energy harvesting application can be found in [37].

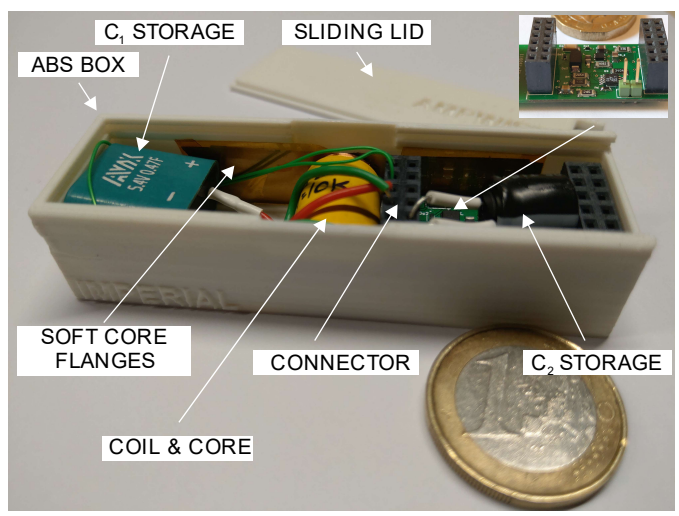

Fig. 4: Photograph of the complete power supply. The sliding lid (shown in the back) has been removed to reveal the system components. A clearer view of the power management PCB is shown in the inset.

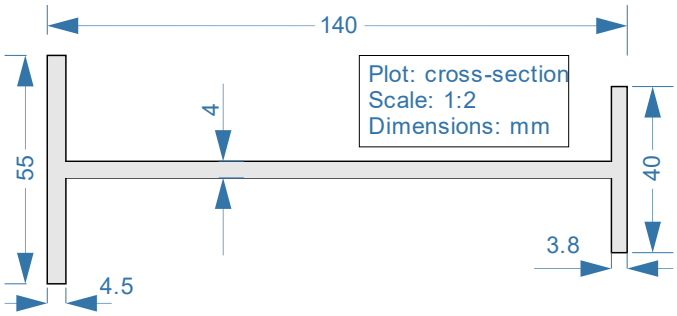

Fig. 5: Cross-section dimensions of the current-carrying beam used as an example application for the power supply characterization.

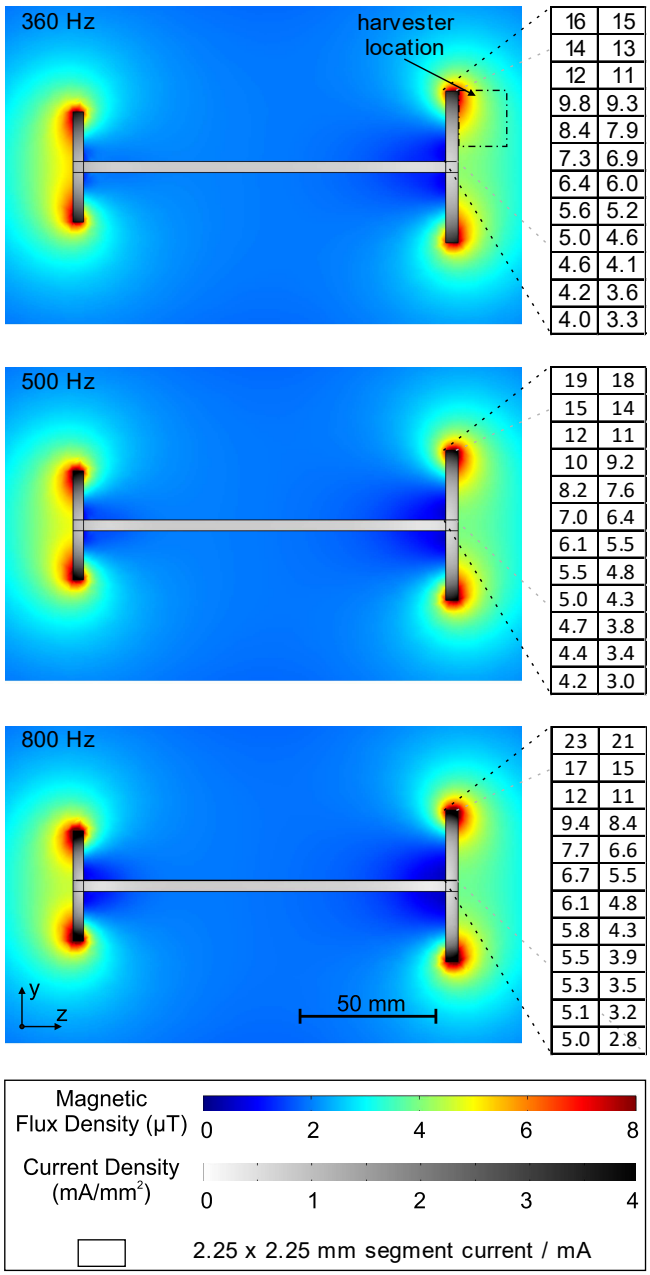

Fig. 6: Simulated J and B amplitude distribution of a 1 A amplitude current running through the beam of Fig. 5. The total current through 2.25 × 2.25 mm segments of the beam cross-section, on one of its four flanges is shown on the side to assist the configuration of an experimental emulation setup.

For laboratory tests, this spatial current distribution of the top-right flange of the H-shaped beam was emulated by multiple rectangular loops of a single current line, distributed in space. A two-dimensional illustration of this testing setup concept is presented in Fig. 7. The loop was chosen to be larger than the device dimensions by at least an order of magnitude to minimize lateral field effects. Regions of higher and lower current densities can be emulated by denser or sparser line passes. In practice, these regions can be configured by segmenting the simulated continuous current density distribution as shown on the side tables of Fig. 6. To emulate the current of each segment, a suitable product of turns times loop current is arranged at the corresponding segment location. The total current along a single flange is 187 mA for 360 Hz, 192 mA for 500 Hz and 199 mA for 800 Hz, corresponding to around 20% of the total bar current of 1 A, for all three cases.

The device prototype of this paper occupies most of the height of a single flange (y-direction in Fig. 6), and the current variation detail along the flange hight has a limited effect to the total flux captured. Therefore, for the emulations the wire loops were dispersed along a height of 25 mm, and the current amplitude was configured to achieve a total current of around 20% of the overall bar current.

As AC current source, a Thurlby Thandar TG5011A function generator with a custom power amplifier and an Agilent 34461A digital multimeter for current feed control were employed. The complete setup is illustrated in Fig. 7. For the characterisation of the transducer in connection with the power management system a Measurement Computing USB-5106 data logger was used, to capture slow supercapacitor charging and discharging effects.

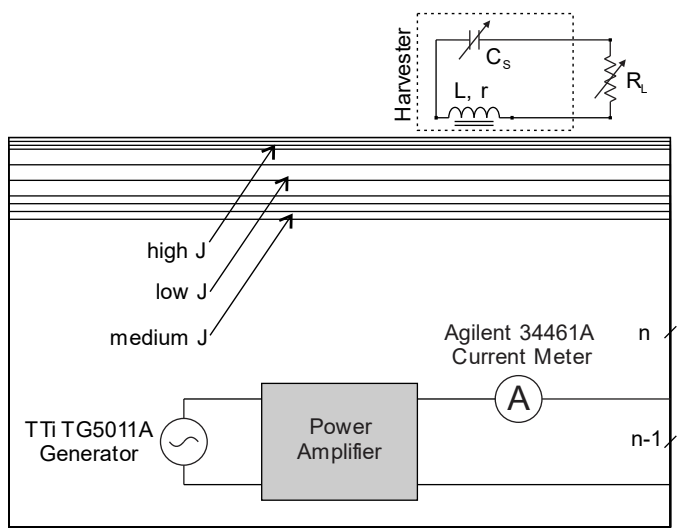

Fig. 7: 2D Illustration of the spatial current distribution emulator.

B. Transducer results

The coil-core transducer described in Section III was tested using the laboratory experimental setup of Section V.B. An indicative photograph of the testing arrangement is shown in Fig. 8. Open circuit coil voltage V_{OC} measurements as a function of structural current for 360 Hz, 500 Hz and 800 Hz are presented as black data points in Fig. 9. As expected from basic induction theory linear scaling of voltage with current is observed. By zero-crossing linear fitting, an open circuit voltage per beam current ratio of 54 mV/A, 73 mV/A and 118 mV/A is obtained, for 360 Hz, 500 Hz and 800 Hz respectively. The corresponding fitting lines are also shown in Fig. 9. Taking into account that commercial power management integrated circuits with input voltage range below 0.5 V are available [8], these results demonstrate that a manageable voltage output can be harvested from a total beam current even below 10 A.

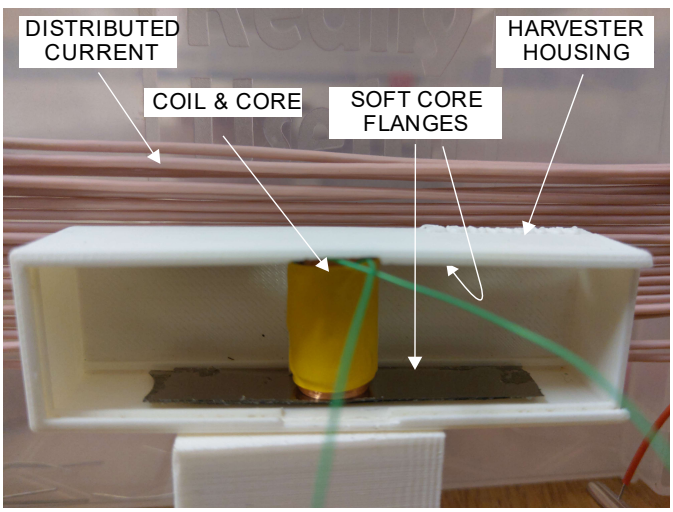

Fig. 8: Photograph of the transducer under laboratory testing.

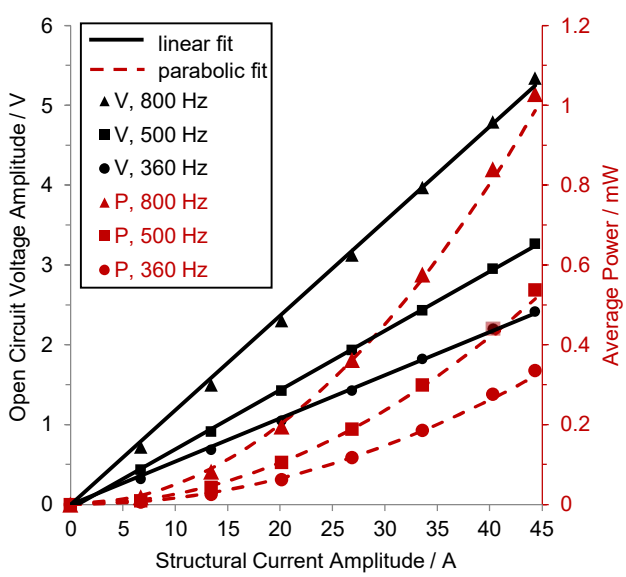

Fig. 9: Experimental open circuit coil voltage vs structural current for three different frequencies. The corresponding output power measured in a separate experimental run on an ohmic load at half-open-circuit voltage conditions is also shown.

In energy harvesting applications, the optimal operating point is typically that of maximal power delivery, which is obtain at impedance matching condition. The coil transducer impedance Z_H includes the coil resistance, a dissipative component due to core eddy currents and the coil reactance. The latter can be countered by a series capacitor C_S connected as shown in the harvester inset of Fig. 7. Tuning C_S such that its reactance is equal to that of the coil impedance L, reduces the output impedance to only its resistive component.

In order to obtain the optimal C_S values for 360 Hz, 500 Hz and 800 Hz, the output impedance of the harvester Z_H, including the coil impedance L, coil resistance r and capacitance C_S was measured by configuring a variable load resistor R_L to a value $R_{L,0}$, such that an output voltage V_L equal to $V_{OC}/2$ is achieved, for different C_S values. This operation point does not correspond to impedance matching, due to the phase of Z_H. Nevertheless, the amplitude of Z_H can be calculated from a measured set of $R_{L,0}$, r and circuit analysis which, for the $V_L = V_{OC}/2$ condition gives:

$$|Z_H| = \sqrt{3 \cdot {R_{L,0}}^2 - 2 \cdot r \cdot R_{L,0}} \tag{2}$$

For r, the measurements presented in section III were used, repeated here for simplicity: 1.6 kΩ, 1.65 kΩ and 1.8 kΩ at 360 Hz, 500 Hz and 800 Hz respectively. For 360 Hz, a minimum Z_H of 2.7 kΩ is obtained by a C_S value of 26 nF. Similarly, for 500 Hz and 800 Hz, the Z_H minimum values are 3.2 kΩ and 4.7 kΩ for 14 nF and 5.2 nF respectively.

In order to measure the power output capability of the energy harvester at each frequency, the corresponding tuning C_S value was used, and the output power voltage was measured on an ohmic load such that $V_L = V_{OC}/2$. If the coil reactance has been completely cancelled by C_S, this corresponds to load matching conditions. The results are plotted as red points back in Fig. 9 as a function of beam current amplitude. As expected, a parabolic increase of power with beam current is observed. Parabolic fitting curves are also plotted as dashed curves. At 45 A beam current amplitude, an average power output of 0.34 mW, 0.54 mW and 1 mW is demonstrated for 360 Hz, 500 Hz and 800 Hz respectively. In practice, the reactance cancellation is imperfect and a significant part of the minimum output impedance specified above is reactive, leading to a slight shift of the maximum power point. This means that a slightly higher power output than demonstrated in Fig. 9 is possible by the device and setup under test.

In the same way, an experimental determination of the C_S values that minimize the harvester impedance for a frequency range between 50 Hz and 800 Hz was performed, including the corresponding output power for a 40 A beam current amplitude. The results are presented in Fig. 10. The frequency dependence of C_S is compared with the theoretically expected from a simple (L, r) inductor model, plotted as a black line in Fig. 10, using an independently measured L value of 5.5 H. The deviation is attributed to non-linearity of core permeability.

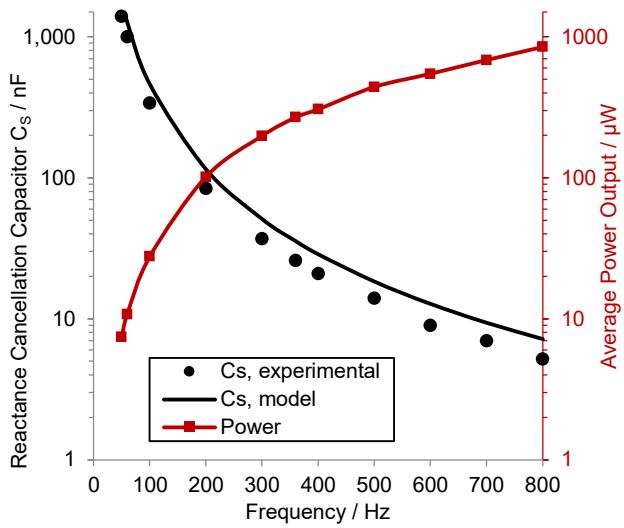

Fig. 10: Experimentally determined reactance cancellation capacitor C_S and corresponding measured output power for a 40 A beam current amplitude. The theoretically expected C_S for a 5.5 H coil inductance is also shown.

At electrical power grid frequency (50 Hz and 60 Hz), the prototype demonstrates 7.5-10 µW of average power from a 40 A distributed beam current amplitude. The corresponding current distributed in each of the four beam flanges is 8 A. This is a promising result towards energy harvesting from electrical installations, where currents of similar amplitude are available at higher spatial densities. The effect of the neutral return current path should be considered in such applications of the proposed device.

In the following section, the transducer characterised here is tested in connection with a custom power management circuit including rectification, storage, boosting and regulation.

C. Power Management results

The energy harvesting transducer was tested in connection with the power management circuit described in Section IV. The transducer was installed in the setup shown in Fig. 8 and the coil output was connected to the circuit input. The testing setup was configured as detailed in Section V.A, for a 40 A amplitude beam current at 360 Hz, 500 Hz and 800 Hz. For each frequency, the optimal value of the reactance cancellation capacitor C_S was used, i.e. 26 nF, 14 nF and 5.2 nF respectively, as obtained by the results of Section V.B. An input storage supercapacitor of C_1 = 0.47 F was used, and an output capacitor of C_2 = 1 mF. The voltage data logger presented a continuous 22 kΩ load to the voltage output V_{OUT}, measured independently by a capacitor discharge experiment.

Experimental results of the voltage at the storage capacitor C_1 and the output capacitor C_2 during cold-starting are presented in Fig. 11. It is noted that the 800 Hz results between the 19th and the 33rd minute are extrapolated from multiple experimental measurements. This is indicated as a light blue curve in Fig. 11. The storage capacitor is getting charged through the voltage doubling Schottky rectifier, with a rate that increases with frequency as expected.

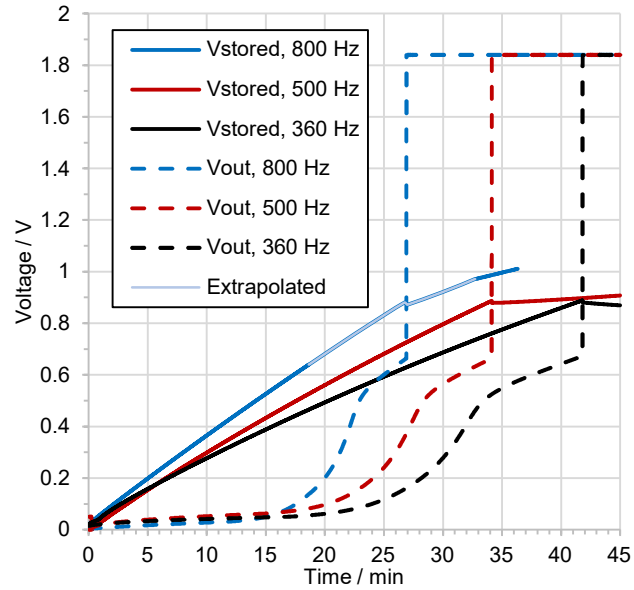

Fig. 11: Experimental measurements of storage and output voltage during cold-starting, in the laboratory measurement setup of Fig. 8, with a 40 A beam current amplitude at three different frequencies.

After reaching around 0.5 V, some charged is leaked to the output allowing an increase of V_{OUT}. When V_{STORE} reaches 0.88 V, the nominal start-up voltage of the MAX17222 booster, the output voltage is enabled and a V_{OUT} = 1.84 V is quickly reached, after a fast charge-pumping stage (not shown) that barely reduces V_{STORE} due to the large C_1/C_2 ratio. The power supply starts-up after 42 min, 34 min and 27 min from 360 Hz, 500 Hz and 800 Hz respectively. Once the power supply is enabled, it provides 0.15 mW to the 22 kΩ data logger input resistance, reducing the V_1 change rate as it can be observed in Fig. 11. In the 360 Hz, this power is larger than the C_1 input power occurring at that V_{STORE} value, and hence C_1 starts discharging.

From the voltage measurements of Fig. 11, the total stored energy and net power can be calculated. The results are presented in Fig. 12 top and bottom respectively. During cold-starting, the input power increases with increasing V_{STORE}. This is because the large initial voltage difference between the coil and C_1 produces a large current and hence large losses on the coil resistance and on the diodes. As V_{STORE} increases, the losses are reduced and the power transfer increases towards a maximum power point. This effect has been studied in [14] for steady-state operation of inductive harvesters, showing that V_{STORE} must be maintained at a specific fraction of the input voltage for maximum coil-to-capacitor power transfer. In the present case this means that the system would benefit from a maximum power point tracking scheme that would tune the charge transfer from C_1 to C_2 such that the optimal V_{STORE} is maintained, both during cold-starting and steady state operation. At the start-up point the system starts supplying the 22 kΩ load with the nominal voltage. The VOUT increases from 0.67 V to 1.84 V, introducing an additional load power of 0.13 mW. This corresponds well with the net power step down observed in Fig. 12 bottom.

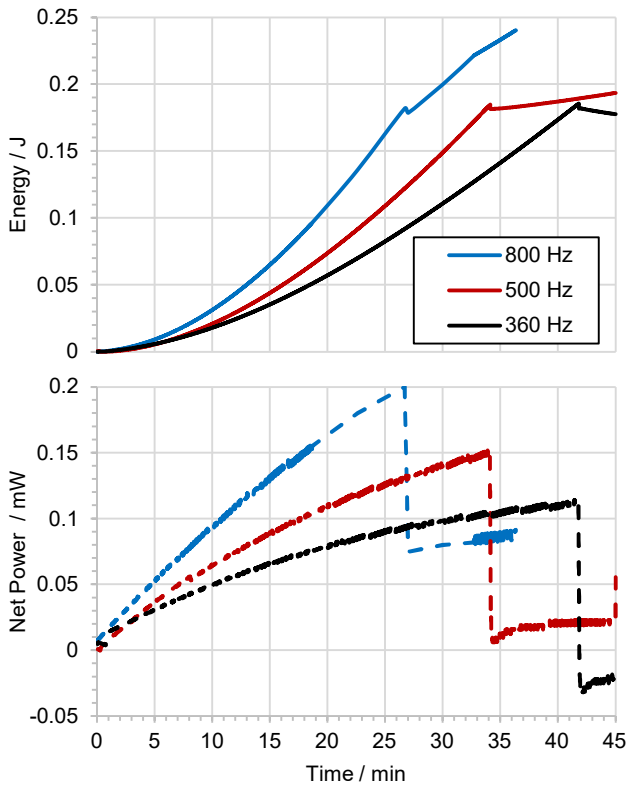

Fig. 12: Experimental stored energy (top) and net power (bottom) calculated from the measurements of Fig. 11.

Furthermore, the system was tested with various ohmic loads connected to its regulated output of 1.84 V, while harvesting energy from the emulated distributed current corresponding to 40 A amplitude of beam current. The results are presented in Fig. 13 top, middle and bottom for a beam current frequency of 360 Hz, 500 Hz and 800 Hz respectively. Because of the harvesting power increase with frequency (due to higher inductive coupling), higher frequencies provided more power income to use. For this reason, a different load sequence scenario was applied during tests for each frequency.

At 360 Hz, the load range used was 22 kΩ – 6.9 kΩ corresponding to 0.15 mW – 0.47 mW, which is higher than the harvested input power. The load is supplied in part by the input and in part by the energy stored on C_1. The stored energy (bold black curve in Fig. 13 top) is reduced with different gradients for each load. Its gradient is the total net power of the power supply, which is shown as a red curve in Fig. 13 top. As mentioned, the coil-to-C_1 power transfer depends on the V_{STORE} status, and as V_{STORE} drops during the experiment, so do the input and net power for a given load. During the first 22 kΩ test (0.15 mW), the net power is -27 µW, corresponding to a 0.13 mW input. During the third 22 kΩ test, the net power is -56 µW, corresponding to a 0.1 mW input. At 6.9 kΩ, the regulated voltage drops to 1.80 V, and the corresponding load power is 0.47 mW. The net power is initially between -0.40 mW and -0.45 mW and drops fast over time as V_{STORE} is further reduced. In the experiments, the booster chip deactivated its regulated output at a falling V_{STORE} of around 0.27 V. This is lower than its nominal low threshold of 0.4 V.

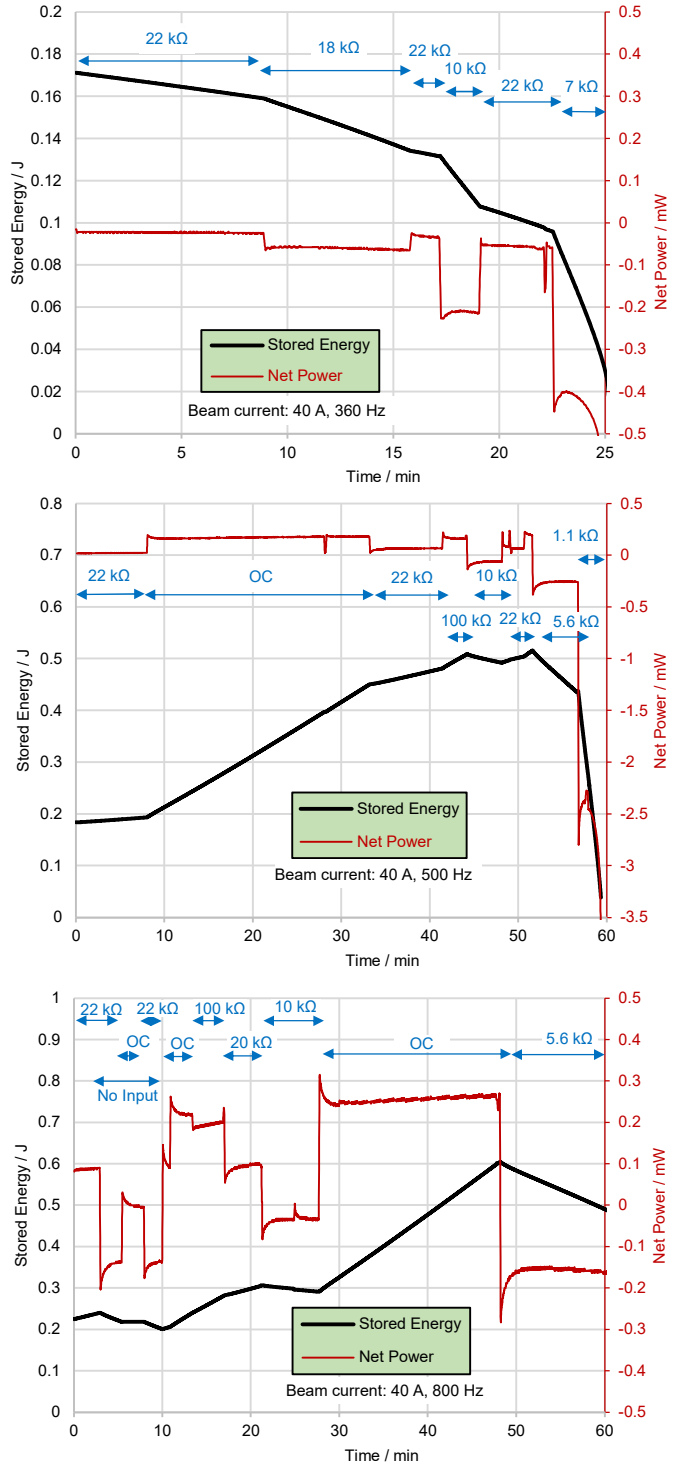

Fig. 13: Experimental stored energy and net power of the power supply in a field corresponding to a 40 A beam current amplitude at 360 Hz (top), 500 Hz (middle) and 800 Hz (bottom), for various ohmic loads connected at the 1.84 V regulated output. Open Circuit conditions are noted as OC.

At 500 Hz, the load range used was 100 kΩ – 1.1 kΩ, corresponding to 0.034 mW – 2.95 mW. At open-circuit conditions (OC in Fig. 13), a 0.17 mW input is observed. This is higher than the corresponding start-up value of Fig. 12, because of the higher V_{STORE}. At 5.6 kΩ (0.58 mW at 1.80 V),

a -0.26 mW net power is observed, which corresponds to 0.32 mW input. This is considerably higher than the value indicated from the OC measurements. The difference may be attributed to higher booster circuit efficiency at higher loads, as well as to more prominent testing-related leakage at open circuit conditions. At the highest used load of 1.1 kΩ (2.95 mW), regulated output is provided for around 3 minutes, largely supported by the stored energy, while the input power is dropping fast with V_{STORE}.

At 800 Hz, the load range used was between 100 kΩ and 5.6 kΩ, corresponding to 0.034 mW – 0.58 mW. The system is first tested on the 22 kΩ (0.15 mW) data logger load, with and without input power. While harvesting, a net power of 90 μW is observed (first 3 mins in Fig. 13 bottom), indicating an input of 0.24 mW. Without input (min 4 to min 10), the system maintains its output and is able to drive the 22 kΩ load, using its stored energy. On a 10 kΩ (0.34 mW) load, a net power of 0.04 mW is observed, indicating a 0.3 mW of input power. The system was then allowed to increase its stored energy at open circuit conditions, demonstrating an input of 0.26 mW. Finally, a 5.6 kΩ (0.58 mW, 1.80 V) load gives a net power of -0.16 mW, which corresponds to 0.42 mW input. Again, this is higher than that obtained during the open circuit measurements, attributed to higher booster efficiency when loaded and more prominent testing-related leakage at open circuit conditions.

The results of this section demonstrate successful cold-starting and provision of regulated power to loads ranging from 0.03 mW to as high as 2.95 mW for several minutes. The maximum demonstrated input power, measured on-storage and on-load, at 360 Hz, 500 Hz and 800 Hz, is 0.13 mW, 0.32 mW and 0.42 mW respectively. In comparison, the corresponding AC power at load-matching conditions is 0.28 mW, 0.44 mW and 0.84 mW, giving a power management efficiency of 46%, 73% and 50% respectively. As these figures were obtained from the overall system power balance, they include rectification, boosting and regulation losses. As noted, the coil-to-C_1 power transfer efficiency depends on V_{STORE} and therefore, better and more consistent efficiency may be possible by implementing a V_{STORE} - control based maximum power point tracking system, with a suitable C_1/C_2 balance [14].

VI. Industrial Testing

A. Description of industrial setup

Further to the laboratory tests performed using the structural beam current distribution emulator presented in the previous section, the transducer and the power supply were also tested on a full-scale aircraft structural beam setup, in the laboratories of a major aircraft manufacturer. The structural beam used has the same H-shape cross-section dimensions with those used in the simulations of Fig. 6, and is part of a larger rig comprising beams, junctions and connections typically used in commercial aircraft. A picture of the energy harvester installed in this application setup is show in Fig. 14.

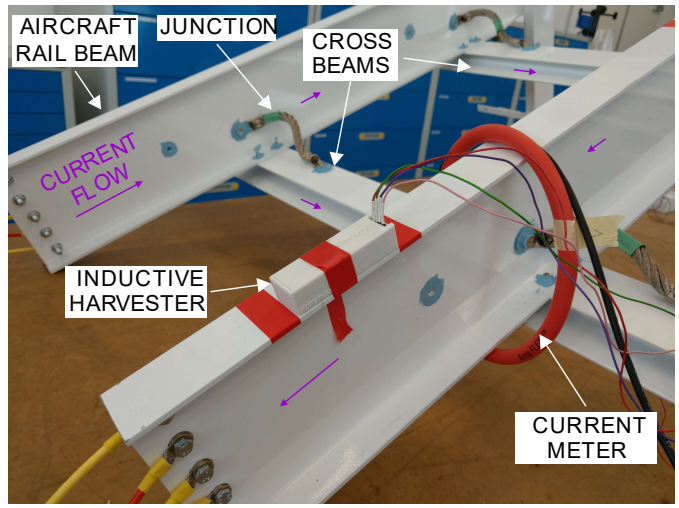

Fig. 14: Photograph of the energy harvesting device under test, installed on an industrial aircraft beam. Purple arrows are used to indicate the current flow direction along the structure.

The beam rig was supplied with currents of various frequencies and amplitudes, by a Chroma 61501 Programmable AC source, through a 1:100 current transformer. The total current was monitored by a loop current meter and controlled manually by configuring the AC source voltage accordingly. The loop current meter was connected to a Rohde & Schwartz RTE 1034, 350 MHz, 5 GSps oscilloscope, through a 8 mV/A Neelogy current to voltage translator. The harvester was tested for a current amplitude range between 5 A and 140 A, for frequencies between 360 Hz and 800 Hz. The harvester open-circuit and loaded voltage output was measured using a TENMA 72-7745 multimeter.

The magnetic field in the vicinity of the harvester installation location was measured, before installation, using a Hirst GM08 Tesla meter. Results for the given beam current range and frequency values are presented in Fig. 15. As expected, a linear increase of flux density with beam current is observed. Zero-crossing linear fits yield 3.70 μT/A, 3.72 μT/A and 3.90 μT/A for 360 Hz, 500 Hz and 800 Hz respectively. These values are within the 3-8 μT/A range produced independently (i.e. without any fitting) by simulation in Fig. 6 across the harvester location. However, they are smaller from the maximum flux density occurring at the beam surface by a factor of two. This can be partly attributed to the 5 mm diameter of the axial probe used for the measurements, which focuses on a few mm away from the surface. It also indicates a somewhat smaller than predicted current concentration to the beam edges. Corresponding measurements on the emulator setup of Fig. 8 demonstrated 2.58-2.64 μT/A at the given frequencies, 30% lower than the industrial beam. An indicative measurement is shown as a green star in Fig. 15. This difference should be taken into account when comparing the harvester performance on the two testbeds.

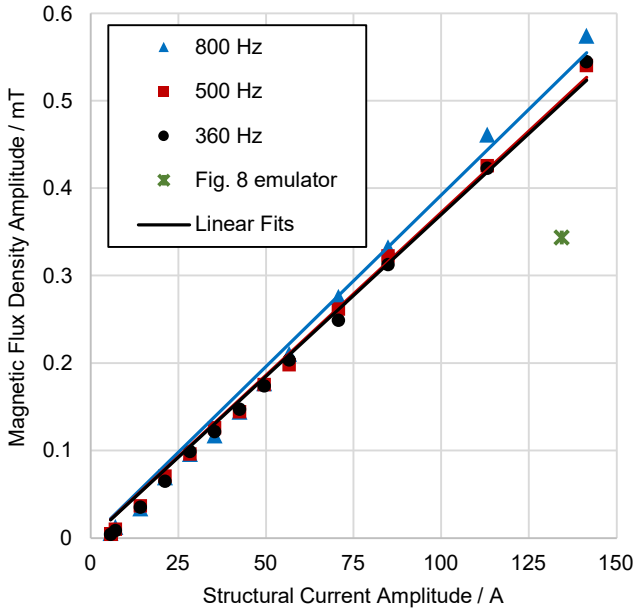

Fig. 15: Measured magnetic flux density at the installation location without the harvester.

B. *Transducer results*

The transducer performance when installed on the beam rig as described in Section VI.A was characterised by measuring the coil output voltage in open circuit and impedance matching conditions. The same approach used in the emulated beam tests of Section V.B was employed. Open circuit coil voltage V_{OC} measurements as a function of structural current for 360 Hz, 500 Hz and 800 Hz are presented as black data points in Fig. 16, along with their zero-crossing linear fitting curves.

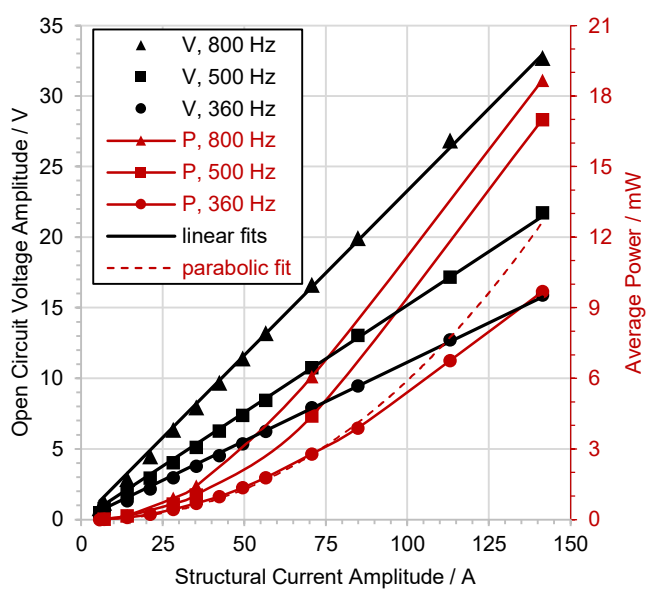

Fig. 16: Experimental open circuit coil voltage vs structural current for three different frequencies, measured on the beam rig of Fig. 14. The corresponding output power measured in a separate experimental run on an ohmic load at half-open-circuit voltage conditions is also shown.

An open circuit voltage per beam current ratio of 112 mV/A, 152 mV/A and 233 mV/A is obtained, for 360 Hz, 500 Hz and 800 Hz respectively. These coupling values are higher than those demonstrated on the emulated spatial current setup of Section V by a factor of two. This is partly due to the 30% lower field achieved by the emulation setup observed in Section V.A. The remaining 20% can be attributed to a larger gap used for device placement in the emulation setup.

The harvester power output was measured, in a separate experimental run, on an ohmic load such that $V_L = V_{OC}/2$. The reactance cancellation capacitor values obtained from the experiments of Section V were used: 26 nF, 14 nF and 5.2 nF for 360 Hz, 500 Hz and 800 Hz respectively. Again, in the case of perfect coil reactance cancellation this corresponds to load matching conditions. The load resistance values the satisfied the $V_L = V_{OC}/2$ condition in this case were 2.6 kΩ, 3.2 kΩ and 5.7 kΩ respectively. These are similar to the ones obtained in Section V. The larger 800 Hz resistance occurred due to a somewhat smaller capacitor value used in practise (4.9 nF).

At 35.4 A beam current amplitude (25 A RMS) an average power output of 0.70 mW, 1.06 mW and 1.43 mW is demonstrated for 360 Hz, 500 Hz and 800 Hz respectively. As before, imperfect reactance cancellation leads to higher output impedance but also to a slight shift of the maximum power point. This means that a slightly higher power output than demonstrated in Fig. 16 is possible by selecting a reactance-matching resistive load, which is different than the one of the $V_L = V_{OC}/2$ condition. For currents larger that 75 A, a deviation of the parabolic power scaling is observed. Indicatively, the 360 Hz parabolic fitting curve is shown as a dashed line in Fig. 16.

In a practical installation, the present power supply will need to operate with a single C_S value, while the beam current frequency may vary. For this reason, the power supply was characterised again, using the 360 Hz tuning C_S for 500 Hz and 800 Hz. The corresponding half-voltage load resistances were found to be 6.5 kΩ and 16.7 kΩ respectively. The results are presented for all three frequencies in Fig. 17 . The output power values for 500 Hz and 800 Hz overlap and are similar to those of the tuned 360 Hz. This is because the output reactance increase is compensated by the voltage increase with frequency. At 35.4 A beam current amplitude (25 A RMS), a minimum of 0.5 mW power supply is demonstrated for all frequencies. These results demonstrate that it is possible to maintain a certain power output through a variable frequency range, by tuning C_S to the minimum frequency. This offers a reduction of output power sensitivity to frequency, which may be advantageous in certain implementations. On the other hand, a more broadband reactance cancellation circuit could allow harvesting energy maximisation at various frequencies, at the expense of more resistive losses introduced by additional needed components.

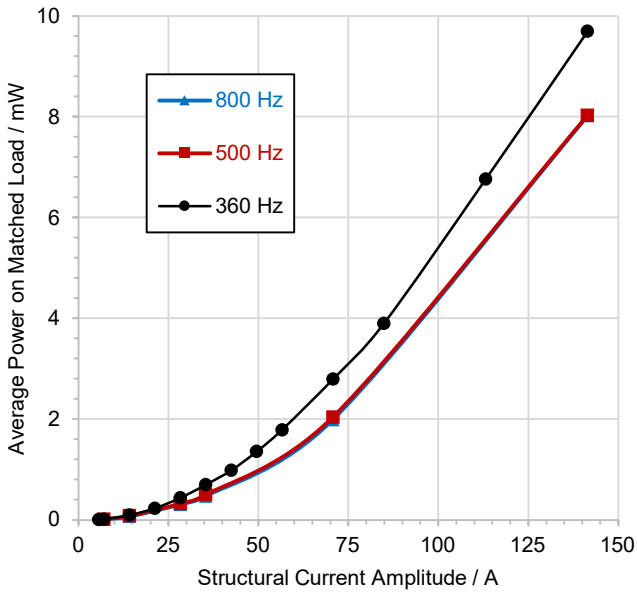

Fig. 17: Experimental comparison of power output at three different frequencies, using the same C_S, tuned to 360 Hz (26 nF). The 500 Hz and 800 Hz results are similar and hence the blue curve is hidden behind the red one.

C. *Power Management results*

The power supply including power management and storage, as described in Section IV, was tested on the industrial beam rig of Fig. 14. Successful cold-starting was demonstrated. The V_{STORED} and V_{OUT} measurements from a 360 Hz, 25 A RMS beam current are presented in Fig. 18. Successful cold starting is demonstrated, after around 20 minutes of energy harvesting. The corresponding power input is also plotted, which is increasing with V_{STORED}. A power of 0.4 mW into C_1 is demonstrated at V_{STORED} = 1.5 V.

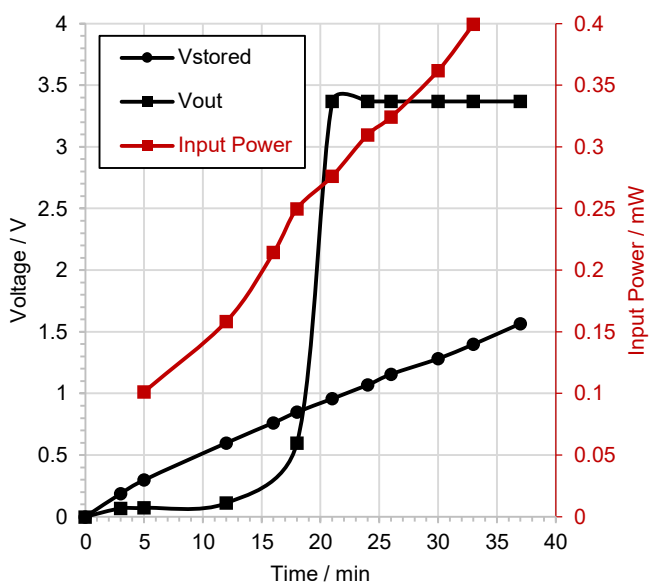

Fig. 18: Cold starting on the industrial beam rig.

VII. Conclusions

The possibility of exploiting the alternating magnetic flux density around current-carrying structures to power wireless sensors was investigated in this paper. The skin effect results in flux concentration at edges, creating privileged installation locations, even at frequencies in the 50 Hz – 1 kHz range, depending on structure size and geometry. Further flux concentration by soft magnetic materials in funnelling shapes can increase the energy harvesting power density by a factor equal to the square of the flux funnelling ratio.

A prototype power supply with a super-capacitor buffer storage was developed using a voltage doubler rectifier and a standard switched inductor - based voltage booster. The power supply was laboratory tested under various consumption loads, demonstrating adequate power provision for duty cycled low power sensor nodes. Further tests were made in an industrial environment, using a testing rig emulating aircraft beams in full scale. A 35.4 A structural current amplitude (25 A RMS) results in a magnetic flux density of around 120 µT at edge locations. A harvested power output of 0.70 mW, 1.06 mW and 1.43 mW is demonstrated for 360 Hz, 500 Hz and 800 Hz respectively. The corresponding power densities per transducer mass are 77 µW/g, 116 µW/g and 157 µW/g, or 0.36 mW/cm^3, 0.54 mW/cm^3 and 0.729 mW/cm^3 per volume.

A direct comparison of performance among power line energy harvesting implementations is difficult due to differences in environmental conditions and testing methods. Nevertheless, a summary of experimental implementations is presented in Table IV. The harvester effect on the primary power line is very small and hence the net output power density is more important than transduction efficiency, as is the case in most harvesting applications. Power densities adequate for supporting wireless sensor nodes in duty cycle operation are demonstrated for all environments. While wrapping the energy harvester around the current source path offers considerable coupling enhancement, this is possible only on specific use cases. Therefore, the installation requirements should be considered when comparing the methods outlined in Table IV.

The study presented here demonstrates a cold-starting power supply, capable of collecting storing and providing regulated output as high as 2.95 mW for several minutes, from spatially distributed currents. Its performance was successfully demonstrated in an industrial environment, opening up the way for energy autonomous wireless multi sensors in the vicinity of distributed currents. Applications include the current return paths in vehicles and electrical infrastructure such as grid installations, power lines as well as electrical rail tracks.

TABLE IV
OVERVIEW OF POWER LINE HARVESTER PROTOTYPES

Paper	Method	Source Line (RMS)	P mW	P_V mW/cm^3
Leland 2006 [22]	Piezo-beam & magnet	13 A, 60 Hz Bipolar	0.35	1.3
Toh 2014 [28]	Tuned coil	0.9 A, 620 Hz	2.9	0.65
He 2014 [20]	Piezo-beam & Halbach array	5 A, 50 Hz Bipolar	0.52	0.21
Yuan 2017 [34]	Bow-tie & helical core	7 µT, 50 Hz	0.61	0.002
White 2018 [29]	Flux Guidance	100 A, 60 Hz	1500	16
Zhuang 2020 [41]	Saturation Countering	10 A, 50 Hz	283	23
This work	Tuned coil, flux funnelling	25 A, 360 Hz Structural	0.70	0.36
This work	Tuned coil, flux funnelling	25 A, 500 Hz Structural	1.06	0.54
This work	Tuned coil, flux funnelling	25 A, 800 Hz Structural	1.43	0.73

Note: P and P_V denote output power and power density per volume.

ACKNOWLEDGEMENTS

This work has received funding from the Clean Sky 2 Joint Undertaking under the European Union's Horizon 2020 research and innovation programme under grant agreement No 785495 and Project AMPWISE. This document reflects only the author's view and the Commission is not responsible for any use that may be made of the information it contains. The authors would like to thank Mr. Samuel K. E. Yang for PCB prototyping work and Dr. Anca Dieudonne, Mr. Damien Laisne and Mr. Christophe Gadal, from Safran Electrical and Power, for preparing and providing the industrial test setup used in this work.

REFERENCES

[1] E. K. Reilly, F. Burghardt, R. Fain, and P. Wright, "Powering a wireless sensor node with a vibration-driven piezoelectric energy harvester," *Smart Materials and Structures,* vol. 20, no. 12, p. 125006, 2011/11/14 2011.

[2] L. v. Allmen *et al.*, "Aircraft Strain WSN powered by Heat Storage Harvesting," *IEEE Transactions on Industrial Electronics,* vol. PP, no. 99, pp. 7284-7292, 2017.

[3] M. Safaei, H. A. Sodano, and S. R. Anton, "A review of energy harvesting using piezoelectric materials: state-of-the-art a decade later (2008-2018)," *Smart Materials and Structures,* vol. 28, no. 11, Nov 2019, Art. no. 113001.

[4] M. R. Sarker, S. Julai, M. F. M. Sabri, S. M. Said, M. M. Islam, and M. Tahir, "Review of piezoelectric energy harvesting system and application of optimization techniques to enhance the performance of the harvesting system," *Sensors and Actuators a-Physical,* vol. 300, Dec 2019, Art. no. Unsp 111634.

[5] J. Choi, I. Jung, and C. Y. Kang, "A brief review of sound energy harvesting," *Nano Energy,* vol. 56, pp. 169-183, Feb 2019.

[6] A. Nozariasbmarz *et al.*, "Review of wearable thermoelectric energy harvesting: From body temperature to electronic systems," *Applied Energy,* vol. 258, Jan 2020, Art. no. 114069.

[7] M. Cansiz, D. Altinel, and G. K. Kurt, "Efficiency in RF energy harvesting systems: A comprehensive review," *Energy,* vol. 174, pp. 292-309, May 2019.

[8] "BQ25505 ultra low-power boost charger with battery management and autonomous power multiplexer for primary battery in energy harvester applications, Texas Instruments," 2019, Available: http://www.ti.com/lit/ds/symlink/bq25505.pdf

[9] "Texas Instruments BQ25570 nano power boost charger and buck converter for energy harvester powered applications," 2019, Available: www.ti.com/product/BQ25570.

[10] Analog, "LTC3109, Auto-Polarity, Ultralow Voltage Step-Up Converter and Power Manager, Datasheet. ," 2018, Available: www.analog.com/en/products/ltc3109.html.

[11] "Linear Technology 3588-1 Nanopower Energy Harvesting Power Supply," 2021, Available: www.analog.com/en/products/ltc3588-1.html.

[12] M. Pollak, L. Mateu, and P. Spies, "Step-up DC-DC-Converter with coupled inductors for low input voltages," *Fraunhofer IIS,* vol. 86, pp. 625-632, 2008.

[13] P. Spies, "Micro Energy Power Management ASIC 2 (ME-PMA2)," Fraunhofer IIS2021, Available: https://www.google.com/url?sa=t&rct=j&q=&esrc=s&source=web&cd=&cad=rja&uact=8&ved=2ahUKEwiwo5LSkY3wAhVZ8LsIHSMkB0sQFjAAegQIBhAD&url=https%3A%2F%2Fwww.iis.fraunhofer.de%2Fcontent%2Fdam%2Fiis%2Fde%2Fdoc%2Flv%2Flos%2Fenergie%2F2012_10_22_Datasheet_DC-DC-ASIC_ME-PMA2.pdf&usg=AOvVaw1iHO80oECJUetQRmBZlwcH.

[14] A. S. Holmes and S. K. E. Yang, "Robust and Highly Efficient Active Rectifier for Low-Voltage Energy Harvesters," *To be published,* 2021.

[15] D. Newell and M. Duffy, "Review of Power Conversion and Energy Management for Low-Power, Low-Voltage Energy Harvesting Powered Wireless Sensors," *IEEE Transactions on Power Electronics,* vol. 34, no. 10, pp. 9794-9805, Oct 2019.

[16] W. He, P. Li, Y. Wen, J. Zhang, C. Lu, and A. Yang, "Energy harvesting from electric power lines employing the Halbach arrays," *Review of Scientific Instruments,* vol. 84, no. 10, p. 105004, 2013.

[17] E. S. Leland, P. K. Wright, and R. M. White, "A MEMS AC current sensor for residential and commercial electricity end-use monitoring," *Journal of Micromechanics and Microengineering,* vol. 19, no. 9, p. 094018, 2009/08/26 2009.

[18] A. Abasian, A. Tabesh, A. Z. Nezhad, and N. Rezaei-Hosseinabadi, "Design Optimization of an Energy Harvesting Platform for Self-Powered Wireless Devices in Monitoring of AC Power Lines," *IEEE Transactions on Power Electronics,* vol. 33, no. 12, pp. 10308-10316, Dec 2018.

[19] A. Abasian, A. Tabesh, N. Rezaei-Hosseinabadi, A. Z. Nezhad, M. Bongiorno, and S. A. Khajehoddin, "Vacuum-Packaged Piezoelectric Energy Harvester for Powering Smart Grid Monitoring Devices," *IEEE Transactions on Industrial Electronics,* vol. 66, no. 6, pp. 4447-4456, Jun 2019.

[20] W. He, P. Li, Y. M. Wen, J. T. Zhang, A. C. Yang, and C. J. Lu, "A Noncontact Magnetoelectric Generator for Energy Harvesting From Power Lines," *IEEE Transactions on Magnetics,* vol. 50, no. 11, Nov 2014, Art. no. 8204604.

[21] T. Hosseinimehr and A. Tabesh, "Magnetic Field Energy Harvesting from AC Lines for Powering Wireless Sensor Nodes in Smart Grids," *IEEE Transactions on Industrial Electronics,* vol. 63, no. 8, pp. 4947-4954, Aug 2016.

[22] E. S. Leland, R. M. White, and P. Wright, "Energy scavenging power sources for household electrical monitoring," in *PowerMEMS*, Berkeley, U.S.A., 2006.

[23] F. Guo, H. Hayat, and Z. Wang, "Energy harvesting devices for high voltage transmission line monitoring," *2011 IEEE Power and Energy Society General Meeting,* pp. 1-8, 2011.

[24] X. Zhao, T. Keutel, M. Baldauf, and O. Kanoun, "Energy harvesting for a wireless-monitoring system of overhead high-voltage power lines," *IET Generation, Transmission & Distribution,* vol. 7, no. 2, pp. 101-107, 2013.

[25] S. Kang, S. Yang, and H. Kim, "Non-intrusive voltage measurement of ac power lines for smart grid system based on electric field energy harvesting," *Electronics Letters,* vol. 53, no. 3, Feb 2017.

[26] J. C. Rodriguez, D. G. Holmes, B. McGrath, and R. H. Wilkinson, "A Self-Triggered Pulsed-Mode Flyback Converter for Electric-Field Energy Harvesting," *IEEE Journal of Emerging and Selected Topics in Power Electronics,* vol. 6, no. 1, pp. 377-386, Mar 2018.

[27] O. Thorin, "Power Line Induction Energy Harvesting Powering Small Sensor Nodes," KTH, School of Industrial Engineering and Management (ITM), Machine Design (Dept.). KTH Royal Institute of Technology, Sweden, 2016.

[28] T. Toh *et al.*, "Inductive energy harvesting from variable frequency and amplitude aircraft power lines," *Journal of Physics: Conference Series,* vol. 557, no. 1, p. 012095, 2014.

[29] R. M. White, D. S. Nguyen, Z. Wu, and P. K. Wright, "Atmospheric Sensors and Energy Harvesters on Overhead Power Lines," *Sensors (Basel),* vol. 18, no. 1, Jan 3 2018.
[30] S. Yuan, Y. Huang, J. Zhou, Q. Xu, C. Song, and P. Thompson, "Magnetic Field Energy Harvesting Under Overhead Power Lines," *IEEE Transactions on Power Electronics,* vol. 30, no. 11, pp. 6191-6202, 2015.
[31] T. Lim and Y. Kim, "Compact Self-Powered Wireless Sensors for Real-Time Monitoring of Power Lines," *Journal of Electrical Engineering & Technology,* vol. 14, no. 3, pp. 1321-1326, May 2019.
[32] B. Park *et al.*, "Optimization design of toroidal core for magnetic energy harvesting near power line by considering saturation effect," *AIP Advances,* vol. 8, no. 5, May 2018, Art. no. 056728.
[33] W. Wang, Z. B. Zhu, Q. Wang, and M. Q. Hu, "Optimisation design of real-time wireless power supply system overhead high-voltage power line," *IET Electric Power Applications,* vol. 13, no. 2, pp. 206-214, Feb 2019.
[34] S. Yuan, Y. Huang, J. Zhou, Q. Xu, C. Song, and G. Yuan, "A High-Efficiency Helical Core for Magnetic Field Energy Harvesting," *IEEE Transactions on Power Electronics,* vol. 32, no. 7, pp. 5365-5376, 2017.
[35] Z. Popovic and B. D. Popovic, "Chapter 20: The Skin Effect," in *Introductory Electromagnetics*: Addison-Wesley, 1999.
[36] S. W. Wright, M. E. Kiziroglou, S. Spasic, N. Radosevic, and E. M. Yeatman, "Inductive Energy Harvesting From Current-Carrying Structures," *IEEE Sensors Letters,* vol. 3, no. 6, pp. 1-4, 2019.
[37] M. E. Kiziroglou, S. W. Wright, and E. M. Yeatman, "Coil and core design for inductive energy receivers," *Sensors and Actuators A: Physical,* vol. 313, p. 112206, 2020/10/01/ 2020.
[38] "Panasonic DB27308 silicon epitaxial planar Schottky Diode specifications," 2021, Available: https://octopart.com/db2730800l-panasonic-44401412.
[39] F. Yuan, *CMOS Circuits for Passive Wireless Microsystems*. Springer Publishing Company, Incorporated, 2011.
[40] (2019). *Maxim Integrated, MAX17220–MAX17225 400mV to 5.5V Input, nanoPower Synchronous Boost Converter with True Shutdown, 19-8753, Rev 4.,* https://www.maximintegrated.com/en/products/power/switching-regulators/MAX17222.html
[41] Y. Zhuang *et al.*, "Improving Current Transformer-Based Energy Extraction From AC Power Lines by Manipulating Magnetic Field," *IEEE Transactions on Industrial Electronics,* vol. 67, no. 11, pp. 9471-9479, Nov 2020.